



**Politecnico
di Torino**

POLITECNICO DI TORINO
CORSO DI LAUREA MAGISTRALE IN
PHYSICS OF COMPLEX SYSTEMS (FISICA DEI SISTEMI COMPLESSI)
A.A. 2022/2023
SESSIONE DI LAUREA OTTOBRE 2023

Dynamical Mean Field Theory for Confluent Tissues and Continuous Constraint Satisfaction Problems

A THESIS AUTHORED BY

Persia Jana Kamali
s304790

BASED ON AN INTERNSHIP AT

**CNRS, CEA, Institut de physique théorique,
F-91191, Gif-sur-Yvette, France**

AND SUPERVISED BY

INTERNAL SUPERVISOR

Alessandro Pelizzola^{1,2,3}

EXTERNAL SUPERVISOR

Pierfrancesco Urbani⁴

¹ *DISAT, Politecnico di Torino, Corso Duca degli Abruzzi 24, I-10129 Torino, Italy*

² *INFN, Sezione di Torino, via Pietro Giuria 1, I-10125 Torino, Italy*

³ *CNR-ISC c/o DISAT, Politecnico di Torino, Corso Duca degli Abruzzi 24, I-10129 Torino, Italy*

⁴ *Université Paris-Saclay, CNRS, CEA, Institut de physique théorique, F-91191, Gif-sur-Yvette, France*

Abstract

Confluent tissues are biological complex systems of interacting and self-propelling cells. Experiments show that such systems undergo phase transitions that play an important role in tissue formation and in the spread of metastatic cancer. Furthermore, the transition shares many properties similar to the jamming transition observed in particulate matter. Inspired by these observations, a model has been proposed where the Voronoi description of confluent tissues is mapped to a random Continuous Constraint Satisfaction Problem (CCSP) with equality constraints: by solving the Hamiltonian with the replica method, the model predicts the same rigidity transition of Vertex/Voronoi models for confluent tissues. In this paper, we re-propose the same model to study the dynamical properties of confluent tissues, under Gradient Descent (GD) and in the mean field limit. With the help of the Dynamical Mean Field Theory (DMFT) description for statistical mechanics, we derive the dynamical equations and we propose an efficient algorithm for their integration. By comparing the results with numerical simulations, we confirm the correctness of the theory and the existence of the rigidity transition observed both experimentally and theoretically. In addition and in the context of optimisation science, we show that GD is blind to Replica Symmetry Breaking (RSB), when it occurs at zero temperature.

Contents

1	Introduction	3
2	The model	4
2.1	Vertex and Voronoi models	4
2.2	Confluent tissues as random CCSP	5
2.3	The dynamics	6
3	Methods	7
3.1	Dynamical Mean Field Theory	7
3.2	Numerical integration	10
3.2.1	Discretisation of DMFT equations	10
3.2.2	Encoding	11
4	Results	12
4.1	Comparison between DMFT and simulation	12
4.2	Results of DMFT's numerical integration	14
5	Digression: gradient descent dynamics and RSB	17
6	Conclusion	17
	References	18

1 Introduction

Biological tissues are complex systems: their macroscopic properties are determined by the collective behaviour of their individual microscopic components, the cells. Rigidity, elasticity, viscosity are all features of a biological tissue that depend on the interaction of cells with their neighbours and the extracellular environment. As in the case of "classical" complex systems, such as a crystal or water, one may expect that also biological tissues can be found in different states of matter, as a consequence of collective behaviour. And this is true: they can be solid, like cartilage and bones, liquid, like blood or gas-like, as mesenchymal cells in embryos [1]. Different phases of tissues can coexist and they can undergo phase transitions. Therefore, one may suggest that also biological tissues can be described by statistical mechanics.

Although concepts like equilibrium, thermodynamical parameters, phase transitions are well-established in statistical physics and successfully describe the macroscopic properties of "inert" materials such as ferromagnets, due to the intrinsic complexity of biological tissues, their theoretical description is far more rich and demanding. While the model for the ideal gas is described by four thermodynamical variables (temperature, pressure, volume, number of molecules), the space of parameters for biological systems is much more large and heterogeneous. Furthermore, what are the control parameters for describing equilibrium and dynamical properties of biological system is not a trivial question, because of the interplay of many processes that involve all scales, from microscopic to macroscopic. Besides one also has to take into account the fact that biological tissues are disordered, meaning that in all states and scales there is a lack of order and symmetry, and active, that is non-conservative inter-cellular forces drive the system in a continuous out-of-equilibrium state. In fact, processes that are restricted inside the cells, like changes in the metabolic network or in the membrane, can have a detectable macroscopic effect, even in the absence of external forces. Nevertheless, developing models capable of reproducing the behaviour of these systems is a fundamental quest for both biologists and physicists, since it promises to bring important advances in understanding the principles of biological life.

Confluent tissues are a thoroughly studied example of biological tissues. They are named after the confluency constraint, since there are no gaps and overlaps between the tissue's cells. Experiments on confluent tissues [2, 3], like the epithelial one, have shown the existence of a phase transition from a fluid-like state, where cell-cell interactions are sparse and cell motility is high, to a solid-like state, where instead interactions increase causing a decrease in cell motility and a collective "solidification". Further research has also shown that such transition plays a role in morphogenesis, the spread of metastatic cancer [4] and in pathogenesis of diseases like asthma [5].

Many theoretical models have tried to explain this rigidity transition in confluent tissues. The most popular and successful ones are Vertex/Voronoi models that describe the tissue as a tessellation of space and consider the fluid-to-solid transition to be cell-shape induced. In fact, cell geometry plays an important role in cell motility: in cellular aggregates, rounded-shape cells tend to move much more slowly than their stretched counterpart. Asthmatic cells, for example, are more elongated than non-asthmatic cells and the rigidity transition for the latter is faster than the one seen in the epithelial tissue of asthmatic donors [5]. Simulations of a simple 3D Vertex model further confirm that the nature of the rigidity transition is purely mechanical: residual stresses that arise due to the impossibility for all cells to reach the target shape cause a "solidification" of the system [6]. The striking feature of the fluid-to-solid transition in confluent tissues is that it shares many properties with jamming transitions observed in particulate matter, where the control parameter is the packing fraction, i.e. the effective volume occupied by the particles [7, 8]. These systems with non-overlapping particles are a standard subject of study in the context of disordered systems and have been essential in understanding the rigidity transition in confluent tissues. An important role in describing these models have been random continuous constraint satisfaction problems (CCSP) and therefore, this led to a study of a simple model of confluent tissues seen as an SAT/UNSAT optimisation problem [9]. By taking the mean field limit, one shows that the phase diagram of this

model is very similar to the ones seen in Vertex/Voronoi models, hence it can be considered as a simple alternative to the standard mean-field models of confluent tissues.

The equilibrium properties of the model in [9] have been largely studied but a dynamical analysis is yet missing. We recall that biological tissues are complex active systems, that are found in a transient state and are continuously driven out of equilibrium due to the fact that cells have self-propulsion. Thus, the study of how such systems behave in out of equilibrium conditions is fundamental to have a global understanding of their properties.

Therefore, the goal of this paper is to study the dynamical behaviour of the model proposed in [9]. Such analysis will be performed in the context of the dynamical mean field theory (DMFT), a powerful tool that will allow us to derive the time-dependence of the observables of the system. We will then discuss how these properties change in the two phases and how this model can be generalised in other contexts. As a final comment, and in the spirit of the interdisciplinary aspect of complex systems, we will address how this model can be useful in studying gradient descent dynamics.

We further remark that the following results are also reported in the preprint [10], where the reader can find a more general DMFT computation.

2 The model

In this section, we will give a brief outline of the models that describe confluent tissues, focusing more on the CCSP model, which is the subject of our study.

2.1 Vertex and Voronoi models

Typical models of confluent tissues describe them as a continuous tessellation of space. The most important ones are Vertex [11] and Voronoi models [12, 13], that differ for how they define such partition. In Vertex models, cells are polygons/polyhedra and the degrees of freedom are the vertices, see Fig. 1a. Instead, in Voronoi models, the degrees of freedom are the centers of the cells, which are built as a Voronoi/Dirichlet construction, see Fig. 1b.

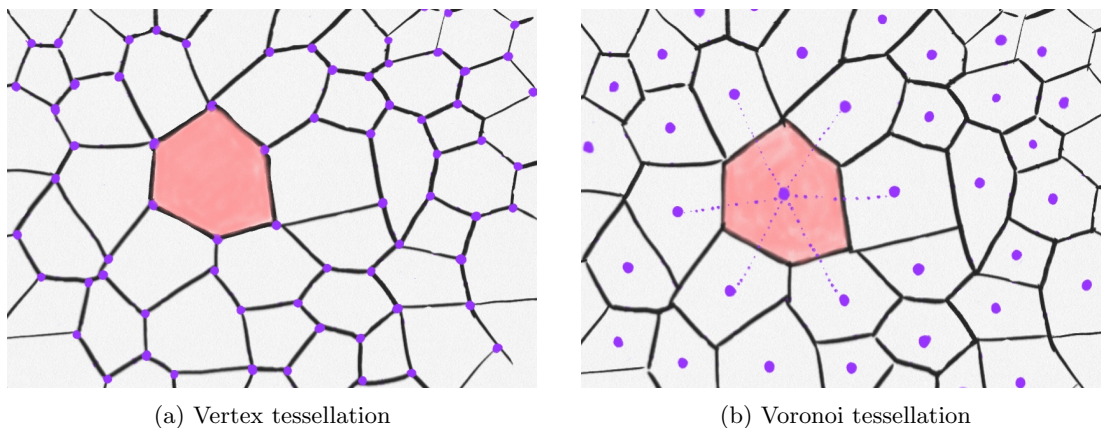


Figure 1: Example of a Vertex and Voronoi tessellation of space. The degrees of freedom are the dots in purple. In Fig. (b) we have highlighted the Voronoi construction.

In both models, confluence is imposed by a geometrical constraint: if all cells attain the target volume and area, then the system is in a liquid or "floppy" state; if at least one cell does not meet the geometrical constraint, then the system is in a solid state. Therefore, the Hamiltonian for both

systems can be written in the following way:

$$H[\mathbf{x}] = \frac{1}{2} \sum_{i=1}^M [k_A (A_i(\mathbf{x}) - A_0)^2 + k_P (P_i(\mathbf{x}) - P_0)^2] \quad (1)$$

where the sum runs over all M cells of the tissue and the degrees of freedom are grouped in \mathbf{x} , a N -dimensional vector. Note that N defines the size of the system, that is the number of degrees of freedom.

The geometrical constraint is represented by A_0 and P_0 , respectively, the target area and perimeter, while the resistance of the cell towards shape deformation is quantified by the elastic constants k_A and k_P . These parameters encode the microscopic properties of the system and take into account the complex interplay of forces, inter-cellular and extra-cellular, that drive the cell to change shape. In particular, the forces that contribute largely to the rigidity transition are cell incompressibility, elasticity of the cellular membrane and the competition between cortical tension and cell-cell adhesion [1, 12, 14].

The control parameter that drives the rigidity transition is the non-dimensionalized preferred perimeter $p_0 = P_0/\sqrt{A_0}$, which depends only on single-cell properties [13]. Therefore, one can define its average value as $p = \langle P \rangle / \sqrt{\langle A \rangle}$, with $\langle P \rangle = \sum_{i=1}^M P_i/M$ and $\langle A \rangle = \sum_{i=1}^M A_i/M$, while by varying p_0 , one can look for the rigidity transition at some critical point p_0^* . For $p_0 > p_0^*$, the system is in a liquid phase: the total energy is at its minimum value, equal to zero, $p = p_0$ and deformations of the tissue have no energetic cost. For $p_0 < p_0^*$, the system is in the solid phase: the energy is positive, $p \neq p_0^*$ and the tissue shows resistance towards deformations. Interestingly, the value of p_0^* is determined by the dimensionality of the system and by its geometrical properties [6].

Note that the number of cells M and the size of the system N are not independent: for a 3D Voronoi model, $N = 3M$, since there are three spatial coordinates for the center of each cell. For a Vertex model, N would be much larger because more than one vertex is associated to each cell. Therefore M and N are related by the relation $M = \alpha N$, where α also plays the role of a control parameter. In fact, systems with confluency constraints have been largely studied well before biological tissues: through constraint counting [8, 15], Maxwell showed that granular systems can solidify when the number of constraints is higher than the number of degrees of freedom ($\alpha > 1$). Instead for under-constrained systems ($\alpha < 1$), a liquid-to-solid rigidity transition is only possible if there is some geometrical constraint on the degrees of freedom [16]. Therefore, we will restrict to the latter case.

2.2 Confluent tissues as random CCSP

According to [9], a similar phase diagram to the one of Vertex/Voronoi models can be obtained from a random continuous constraint satisfaction problem (CCSP) with equality constraints.

Constraint satisfaction problems are known in optimisation science as problems where a set of degrees of freedom have to satisfy a set of constraints [17]: if at least one set of degrees of freedom that satisfies all the constraints exists, then the problem is said to be satisfiable (SAT); otherwise, it is said to be unsatisfiable (UNSAT). A continuous constraint satisfaction problem is a satisfaction problem where the degrees of freedom can take values in the real domain; a random constraint satisfaction problem has random constraints. Note that such constraints can either be equality constraints or inequality constraints. CCSPs have played a great role in describing the mean field limit of systems of non-overlapping particles [18] and have successfully predicted the statistical features of their rigidity transition.

The model in [9] is the following: we consider a N -dimensional vector $\mathbf{x} = \{x_1, x_2, \dots, x_N\}$ constrained on a sphere, $|\mathbf{x}^2| = N$, that defines a compact phase space. The area and perimeter constraints in Vertex/Voronoi models are replaced by a set of M non-linear random functions $h_\mu(\mathbf{x})$. We consider p_0 as the control parameter and we will refer to it as the target index shape. Note

that it has not the same definition as above but it has the same role. Thus the energy of the model becomes:

$$H[\mathbf{x}] = \frac{1}{2} \sum_{\mu=1}^M (h_{\mu}(\mathbf{x}) - p_0)^2 \quad (2)$$

where $M = \alpha N$ with $\alpha < 1$. Parameters M and N are still, respectively, the number of the cells and the size of the system. The random functions have form

$$h_{\mu}(\mathbf{x}) = \frac{1}{N} \sum_{i < j}^N J_{ij}^{\mu} x_i x_j \quad \mu = 1, \dots, M \quad (3)$$

and each $h_{\mu}(\mathbf{x})$ is identified by a $N \times N$ random matrix J_{ij}^{μ} , whose entries are i.i.d. random Gaussian variables with zero mean and unit variance. In addition, we will consider the symmetry $J_{ij}^{\mu} = J_{ji}^{\mu}$.

Although this model is abstract and has no microscopical derivation, it is simple enough to be exactly soluble in the mean field limit and, more importantly, has a very similar phase diagram to the ones of Voronoi/Vertex models. By computing the partition function of the model with the replica method and then performing a saddle point, see [9] for the detailed calculation, one finds the following results for $\alpha = 0.25$ and zero temperature:

- The liquid/SAT to solid/UNSAT transition happens for a value of $p_0 = p_J \simeq 1.871$. Note that the transition occurs by increasing p_0 , as opposed to the case of Vertex/Voronoi models.
- The existence of a replica symmetry breaking at $p_0 = p_0^G = 1$ that divides the liquid/SAT phase into two regions: for $p_0 < p_0^G$, the liquid is replica symmetric and behaves as "classical" statistical system; for $p_0^G < p_0 < p_J$, the system is in a liquid-glassy phase and shares properties similar to amorphous solids in the Gardner phase. Therefore, the solid/UNSAT phase is always in a glassy state.

2.3 The dynamics

Since the equilibrium properties of model in Eq. (2) have been thoroughly studied in [9], in this paper we are interested in its dynamical properties at zero temperature and for $\alpha = 0.25$.

In statistical mechanics, systems of many interacting parts are describe by a point in phase space that moves in time. A way to describe out-of-equilibrium properties is to imagine that the system moves in a free energy landscape of the system according to a Langevin dynamics, which is simply a generalisation of Newton's equation for systems in contact with a thermal bath:

$$\dot{x}_i(t) = -\mu(t)x_i(t) - \frac{\partial H}{\partial x_i(t)} + \xi_i(t) \quad i = 1, \dots, N \quad (4)$$

where $\mu(t)$ is the Lagrange multiplier that enforces the constraint $|\mathbf{x}(t)|^2 = N$ and $\xi(t)$ is a Gaussian random variable that quantifies the dissipative effect of the thermal bath. For our model, we will consider the dynamics at zero temperature by omitting the noise term:

$$\dot{x}_i(t) = -\mu(t)x_i(t) - \frac{\partial H}{\partial x_i(t)} \quad i = 1, \dots, N \quad (5)$$

For a generalisation of this model for non-zero noise, see [10].

To study the dynamics, we are interested in the time-dependence of the following observables:

- The correlation function

$$C(t, t') = \frac{1}{N} \langle \mathbf{x}(t) \mathbf{x}(t') \rangle \quad (6)$$

A two-time quantity that measures the correlation between two different configurations of the system at two different times.

- The instantaneous linear response function

$$R(t, t') = \left. \frac{\delta \langle \mathbf{x}(t) \rangle}{\delta \eta(t')} \right|_{\eta=0} \quad t > t' \quad (7)$$

Another two-time quantity that measures the response of the system in a state \mathbf{x} at time t to a linear perturbation η that happened at time t' .

- The average energy per degree of freedom

$$e(t) = \frac{1}{N} \langle H(t) \rangle \quad (8)$$

- The average value of $h_\mu(t)$

$$h(t) = \frac{1}{M} \sum_{\mu=0}^M \langle h_\mu(t) \rangle \quad (9)$$

Note that by $\langle \cdot \rangle$ we mean the average over the initial condition $\mathbf{x}(0)$, the disorder introduced by the matrices J_{ij} and, if present, the noise $\xi(t)$.

3 Methods

In this section we will discuss the theoretical methods and analytical tools used to derive the dynamical properties of the model in Eq. (2). We will then continue the discussion by proposing a method for the numerical integration of the differential equations obtained from the theory.

3.1 Dynamical Mean Field Theory

To compute the observables above, one would need to solve the N dependent differential equations for $x_i(t)$, an impossible task if N is very large. Therefore, instead of solving explicitly the differential equations, we will consider a more intelligent route by taking advantage of the mean field nature of our model and by applying Dynamical Mean Field Theory (DMFT). This approach will lead us to a set of closed integro-differential equations for $C(t, t')$ and $R(t, t')$, which can be then easily integrated numerically. This is where lies the power of the mean field theory: instead of solving N dependent Langevin equations, we simply solve two integro-differential equations.

In any system described by a Langevin equation, all averaged observable $\langle A[q] \rangle(t)$ can be compute through the dynamic generating functional \mathcal{Z}_{dyn} [19]:

$$\langle A[\mathbf{x}] \rangle(t) = \left. \frac{\delta \mathcal{Z}_{dyn}}{\delta \eta(t)} \right|_{\eta(t)=0} \quad (10)$$

$$\mathcal{Z}_{dyn} = \int \mathcal{D}\xi P[\xi] \exp \left(\int dt' \eta(t') A[\mathbf{x}^{sol}](t') \right) \Big|_{\eta(t)=0} \quad (11)$$

where $\eta(t)$ is a time-dependant source, $\mathbf{x}^{sol}(t)$ is the solution of the Langevin dynamics in Eq. (4) and $P[\xi]$ is the probability distribution of the noise, which in our case can be considered as a delta Dirac function in zero, since we are omitting it. Note that $\mathcal{Z}_{dyn}[\eta = 0] = 1$ because $P[\xi]$ is normalized. If disorder is present, one should also average \mathcal{Z}_{dyn} over its probability distribution and, since $\mathcal{Z}_{dyn}[\eta = 0] = 1$, this can be done easily, without using the replica method. Therefore, the dynamic generating functional encodes the relevant properties of the dynamics and dynamical mean field theory will be essential in its evaluation.

In this paper, we will compute \mathcal{Z}_{dyn} with the Martin-Siggia-Rose-Jenssen-De Dominicis approach and use the supersymmetry (SUSY) formalism for stochastic processes [19, 20], that will be useful to write the dynamic generating function in a compact form. The calculation will follow the ones in papers [21, 22, 23] and note that we will omit all irrelevant constant factors.

The derivation starts with the Martin-Siggia-Rose-Jenssen-De Dominicis identity:

$$1 = \mathcal{Z}_{dyn} = \left\langle \int \mathcal{D}\mathbf{x}(t) \prod_{i=1}^N \delta \left(-\dot{x}_i(t) - \mu(t)x_i(t) - \frac{\partial H}{\partial x_i(t)} \right) \right\rangle. \quad (12)$$

We then re-write the equation with the SUSY algebra by introducing a set of Grassmann variables θ_a, θ_b and the super-field $\mathbf{x}(a) = \mathbf{x}(t_a) + i\theta_a \hat{\mathbf{x}}(t_a)$ [24]. The idea of the SUSY formalism is to enlarge the dimension of time such that an instant t_a corresponds to a multidimensional variable $a = (t_a, \theta_a)$.

By averaging over the J_{ij}^μ s and performing a variable change, the SUSY formulation of \mathcal{Z}_{dyn} becomes

$$\mathcal{Z}_{dyn} = \int \mathcal{D}Q(a, b) \exp(N\mathcal{A}_{dyn}[Q]) \quad (13)$$

$$\mathcal{A}_{dyn}[Q] = -\frac{1}{2} \int da db \mathcal{K}(a, b) Q(a, b) + \frac{1}{2} \ln \det(Q) + \alpha \ln Z_{loc} \quad (14)$$

where $\mathcal{K}(a, b)$ is the kinetic kernel and $Q(a, b)$ is the dynamical overlap matrix,

$$Q(a, b) = \frac{\mathbf{x}(a) \cdot \mathbf{x}(b)}{N}. \quad (15)$$

Z_{loc} is the partition function of the impurity problem $h(a) = h(\mathbf{x}(a))$ and one can easily show that

$$Z_{loc} = \det(I + G)^{-\frac{1}{2}} \exp\left(\frac{p_0^2}{2} \int da db [G^{-1} + I]^{-1}(a, b)\right), \quad (16)$$

where the operator G is defined as $G(a, b) = \frac{Q(a, b)^2}{2}$.

In DMFT derivations, Z_{loc} defines an effective stochastic process where the dynamics is non-Markovian. Usually, in order to evaluate the DMFT equations, one has to extract the dynamics of the local problem and then numerically integrate it, see [21, 22, 23]. In this special case, due to a quadratic energy function, the local partition function is simply a Gaussian integral and it is easy to solve.

At this point of the calculation, we introduce the mean field approximation and evaluate the dynamical partition function with the saddle point method

$$\mathcal{Z}_{dyn} = \int \mathcal{D}Q(a, b) \exp(N\mathcal{A}_{dyn}[Q]) \xrightarrow{N \rightarrow \infty} \exp(N\mathcal{A}_{dyn}[Q^*]) \quad (17)$$

where Q^* is such that

$$\frac{\delta}{\delta Q(a, b)} \mathcal{A}_{dyn}[Q] \Big|_{Q^*} = 0 \quad (18)$$

$$-\frac{1}{2} \mathcal{K}(a, b) + \frac{1}{2} Q^{-1}(a, b) + \alpha \frac{\delta \ln Z_{loc}}{\delta Q(a, b)} \Big|_{Q^*} = 0. \quad (19)$$

Note that at the saddle point $\langle Q(a, b) \rangle_{\mathcal{Z}_{dyn}} = Q^*(a, b)$. By recalling the definition of $Q(a, b)$ and $\mathbf{x}(a)$, we have that

$$\begin{aligned} \langle Q(a, b) \rangle_{\mathcal{Z}_{dyn}} &= \frac{\langle \mathbf{x}(a) \cdot \mathbf{x}(b) \rangle}{N} \\ &= \frac{\langle \mathbf{x}(t_a) \cdot \mathbf{x}(t_b) \rangle}{N} + \theta_a \frac{\langle \mathbf{x}(t_b) \cdot i\hat{\mathbf{x}}(t_a) \rangle}{N} + \theta_b \frac{\langle \mathbf{x}(t_a) \cdot i\hat{\mathbf{x}}(t_b) \rangle}{N} \\ &\quad + \theta_a \theta_b \frac{\langle i\hat{\mathbf{x}}(t_a) \cdot i\hat{\mathbf{x}}(t_b) \rangle}{N} \end{aligned} \quad (20)$$

and considering that the symmetries of the SUSY group imply that the dynamics is causal

$$\langle i\hat{\mathbf{x}}(t_a) \cdot i\hat{\mathbf{x}}(t_b) \rangle = 0, \quad (21)$$

one can observe that $Q^*(a, b)$ encodes the observables of interest:

$$Q^*(a, b) = C(t_a, t_b) + \theta_a R(t_b, t_a) + \theta_b R(t_a, t_b). \quad (22)$$

In fact, one can show that $R(t_a, t_b) = \frac{\langle \mathbf{x}(t_a) \cdot i\hat{\mathbf{x}}(t_b) \rangle}{N}$, see [19] for a derivation. Returning to Eq. (19), one can compute explicitly the derivative of Z_{loc} with respect to $Q(a, b)$ and then multiply the left hand side by $Q(c, b)$ and integrate over c :

$$\begin{aligned} & - \int dc \mathcal{K}(a, c) Q(c, b) + \delta(a - b) - \alpha \int dc (I + G)^{-1}(a, c) Q(a, c) Q(c, b) + \\ & + \alpha p_0^2 \int dc dx dy Q(a, c) (I + G)^{-1}(x, a) (I + G)^{-1}(y, c) Q(c, b) = 0. \end{aligned} \quad (23)$$

Before unpacking the SUSY algebra, we first re-write the operator $(I + G)^{-1}$ in the following way

$$A(a, b) = (I + G)^{-1}(a, b) = C_A(t_a, t_b) + \theta_a R_A(t_b, t_a) + \theta_b R_A(t_a, t_b) \quad (24)$$

and from Eq. (23), we finally derive the integro-differential equations for $C(t, t')$ and $R(t, t')$, known in the literature as Schwinger-Dyson equations or DMFT equations:

$$\begin{aligned} \partial_t C(t, t') &= -\mu(t) C(t, t') + \\ & - \alpha \int_0^{t'} dt' C_A(t, t'') C(t, t'') R(t', t'') + \\ & - \alpha \int_0^t dt'' [C_A(t, t'') R(t, t'') C(t'', t') + R_A(t, t'') C(t, t'') C(t'', t')] + \\ & + \alpha p_0^2 \int_0^{t'} dt'' \int_0^t dt_x \int_0^{t''} dt_y R_A(t, t_x) R_A(t'', t_y) C(t, t'') R(t', t'') + \\ & + \alpha p_0^2 \int_0^{t'} dt'' \int_0^t dt_x \int_0^{t''} dt_y R_A(t, t_x) R_A(t'', t_y) R(t, t'') C(t'', t') \end{aligned} \quad (25)$$

$$\begin{aligned} \partial_t R(t, t') &= -\mu(t) R(t, t') + \delta(t - t') + \\ & - \alpha \int_{t'}^t dt'' [C_A(t, t'') R(t, t'') R(t'', t') + R_A(t, t'') C(t, t'') R(t'', t')] + \\ & + \alpha p_0^2 \int_{t'}^t dt'' \int_0^t dt_x \int_0^{t''} dt_y R_A(t, t_x) R_A(t'', t_y) R(t, t'') R(t'', t'). \end{aligned} \quad (26)$$

Note that we took into account causality, that is for $t' > t$ the linear response function is $R(t, t') = 0$ and also $R_A(t, t') = 0$.

The equation for $\mu(t)$ is derived from the equation of $C(t, t')$ by imposing $\partial_t C(t, t) = 0$:

$$\begin{aligned} \mu(t) &= -\alpha \int_0^t dt'' [2C_A(t, t'') C(t, t'') R(t, t'') + R_A(t, t'') C(t, t'')^2] + \\ & + 2\alpha p_0^2 \int_0^t dt'' \int_0^t dt_x \int_0^{t''} dt_y R_A(t, t_x) R_A(t'', t_y) C(t, t'') R(t, t''). \end{aligned} \quad (27)$$

Finally, what are left to derive are the equations for $C_A(t, t')$ and $R_A(t, t')$ in terms of $C(t, t')$ and $R(t, t')$. One does this by starting from the following relation

$$\int dc A(a, c)(I + G)(c, b) = \delta(a - b) \quad (28)$$

and then by substituting the definition of the operator G . The equation that one obtains is

$$\int dt_c \mathcal{M}(t_b, t_c) \begin{pmatrix} C_A(t_a, t_c) \\ R_A(t_a, t_c) \end{pmatrix} = \begin{pmatrix} 0 \\ \delta(t_a - t_b) \end{pmatrix}, \quad (29)$$

where the matrix \mathcal{M} has entries

$$\mathcal{M}(t_b, t_c) = \begin{pmatrix} \delta(t_c - t_b) + C(t_c, t_b) R(t_b, t_c) & \frac{1}{2} C(t_c, t_b)^2 \\ R(t_b, t_c) R(t_c, t_b) & \delta(t_c - t_b) + C(t_c, t_b) R(t_c, t_b) \end{pmatrix}. \quad (30)$$

Therefore, in order to compute C_A and R_A one has to perform the inversion of the operator on the left hand side of Eq. (29). Note that, again due to causality, $R(t_b, t_c)R(t_c, t_b) = 0$.

3.2 Numerical integration

As one can clearly see, the Schwinger-Dyson equation cannot be solved analytically and one must opt for a numerical integration. This is straightforward: again due to causality, to find the value of $C(t, t')$ and $R(t, t')$ at the next time step, one only needs the values of $C(t, t')$, $R(t, t')$, $C_A(t, t')$, $R_A(t, t')$ in the past. The only difficulty lies in understanding how to re-write Eq. (29) in a more algorithmically accessible form.

3.2.1 Discretisation of DMFT equations

Before performing the numerical integration of the DMFT equations, we must first discretise them. Therefore, we divide time into L slices of size Δt and C , R , C_A , R_A become L^2 -dimensional matrices. To address the elements of these matrices, we will use the following notation:

$$C_{t_a, t_b} = C(t = t_a \Delta t, t' = t_b \Delta t), \quad t_a, t_b = 0, 1, \dots, L - 1.$$

The discretisation of the Schwinger-Dyson equations is simple:

$$\begin{aligned} C_{t_a+1, t_b} - C_{t_a, t_b} &= \Delta t \left\{ -\mu_{t_a} C_{t_a, t_b} + \right. \\ &\quad - \Delta t \alpha \sum_{t''=0}^{t_b} C_{t_a, t''}^A C_{t_a, t''} R_{t_b, t''} + \\ &\quad - \Delta t \alpha \sum_{t''=0}^{t_a} (C_{t_a, t''}^A R_{t_a, t''} C_{t'', t_b} + R_{t_a, t''}^A C_{t_a, t''} C_{t'', t_b}) + \\ &\quad + \Delta t^3 \alpha p_0^2 \sum_{t''=0}^{t_b} \left[\left(\sum_{t_x=0}^{t_a} R_{t_a, t_x}^A \right) \left(\sum_{t_y=0}^{t''} R_{t'', t_y}^A \right) C_{t_a, t''} R_{t_b, t''} \right] + \\ &\quad \left. + \Delta t^3 \alpha p_0^2 \sum_{t''=0}^{t_a} \left[\left(\sum_{t_x=0}^{t_a} R_{t_a, t_x}^A \right) \left(\sum_{t_y=0}^{t''} R_{t'', t_y}^A \right) R_{t_a, t''} C_{t'', t_b} \right] \right\} \quad (31) \end{aligned}$$

$$\begin{aligned}
R_{t_a+1,t_b} - R_{t_a,t_b} = & \delta_{t_a,t_b} + \Delta t [-\mu_{t_a} R_{t_a,t_b} + \\
& - \Delta t \alpha \sum_{t''=t_b}^{t_a} (C_{t_a,t''}^A R_{t_a,t''} R_{t'',t_b} + R_{t_a,t''}^A C_{t_a,t''} R_{t'',t_b}) + \\
& + \Delta t^3 \alpha p_0^2 \sum_{t''=t_b}^{t_a} \left(\sum_{t_x=0}^{t_a} R_{t_a,t_x}^A \right) \left(\sum_{t_y=0}^{t_a} R_{t'',t_y}^A \right) R_{t_a,t''} R_{t'',t_b} \Big]. \quad (32)
\end{aligned}$$

While for the Lagrange multiplier we have that:

$$\begin{aligned}
\mu_{t_a} = & -\Delta t \alpha \sum_{t''=0}^{t_a} [2C_{t_a,t''}^A C_{t_a,t''} R_{t_a,t''} + R_{t_a,t''}^A C_{t_a,t''}^2 + \\
& -2\Delta t^2 p_0^2 \left(\sum_{t_x=0}^{t_a} R_{t_a,t_x}^A \right) \left(\sum_{t_y=0}^{t''} R_{t'',t_y}^A \right) R_{t_a,t''} C_{t'',t_a} \Big]. \quad (33)
\end{aligned}$$

We also discretise the equation for C_A and R_A :

$$\sum_{t_c=0}^{L-1} \Delta t \begin{pmatrix} \frac{\delta_{t_c,t_b}}{\Delta t} + C_{t_c,t_b} R_{t_b,t_c} & \frac{1}{2} C_{t_c,t_b}^2 \\ R_{t_b,t_c} R_{t_c,t_b} & \frac{\delta_{t_c,t_b}}{\Delta t} + C_{t_c,t_b} R_{t_c,t_b} \end{pmatrix} \begin{pmatrix} C_{t_a,t_c}^A \\ R_{t_a,t_c}^A \end{pmatrix} = \begin{pmatrix} 0 \\ \frac{\delta_{t_a,t_b}}{\Delta t} \end{pmatrix}. \quad (34)$$

3.2.2 Encoding

As previously said, the difficulty in solving numerically the DMFT equations lies in the tensorial form of the equations for C_A and R_A . In order to be able to perform an operator inversion, one could look for a mapping between the original operator in Eq. (34) and a matrix with two axis, instead of three. In other words, we would like to re-write equation Eq. (34) in the following way:

$$\forall t_a = 0, 1, \dots, L-1 \quad \sum_{k'=0}^{2L-1} \Lambda_{kk'} v_{k'}(t_a) = w_k(t_a) \quad (35)$$

such that at each t_a we compute C_A and R_A by simply inverting matrix Λ .

In the following sections, we will show two different ways how to perform this mapping.

Encoding 1 A direct encoding for the equation is the following: we define two super-indices k and k' that depend on two sub-indexes (σ, t_b) and we write that

$$\begin{aligned}
k = k(\sigma, t_b) = 2t_b + \sigma & \quad k' = k'(\sigma', t_c) = 2t_c + \sigma' \\
t_b, t_c = 0, 1, \dots, L-1 & \quad \sigma, \sigma' = 0, 1.
\end{aligned} \quad (36)$$

Note that (σ, σ') simply tells which element of the 2×2 matrix $\mathcal{M}(t_b, t_c)$ we are considering.

The relation between k and (t_b, σ) is bijective, so given k , we have that:

$$t_b, t_c = \left\lfloor \frac{k}{2} \right\rfloor \quad \sigma = k \bmod 2. \quad (37)$$

Finally, we have that Λ is a $4L^2$ -dimensional matrix and \mathbf{v}, \mathbf{w} are $2L$ -dimensional vectors with the

following entries:

$$\Lambda_{k(\sigma, t_b), k'(\sigma', t_c)} = \{\delta_{t_c, t_b} + \Delta t C_{t_c, t_b} [R_{t_b, t_c} (1 - \sigma) + R_{t_c, t_b} \sigma]\} (1 - |\sigma - \sigma'|) + \frac{1}{2} \Delta t C_{t_c, t_b}^2 \sigma' |\sigma - \sigma'| \quad (38)$$

$$v_{k'(\sigma', t_c)}(t_a) = C_{t_a, t_c}^A (1 - \sigma') + R_{t_a, t_c}^A \sigma' \quad (39)$$

$$w_{k(\sigma, t_b)}(t_a) = \frac{\delta_{t_a, t_b}}{\Delta t} \sigma. \quad (40)$$

Encoding 2 The following encoding allows one to have a very efficient code: at each t_a the inverse of Λ is computed in a recursive way. In fact, one can show that Λ is a block matrix, that inherits the upper triangular structure of $\mathcal{M}(t_b, t_c)$. By taking $(k, k') = (t_c, t_b)$, the encoding is the following:

$$\Lambda_{t_c, t_b} = \begin{cases} \delta_{t_c, t_b} + \Delta t C_{t_c, t_b} R_{t_b, t_c} & t_c, t_b < L \\ \delta_{t_c, t_b} + \Delta t C_{t_c, t_b} R_{t_c, t_b} & t_c, t_b \geq L \\ 0 & t_c \geq L, t_b < L \\ \frac{1}{2} \Delta t C_{t_c, t_b}^2 & t_c < L, t_b \geq L \end{cases} \quad (41)$$

$$v_{t_c}(t_a) = \begin{cases} C_{t_a, t_c}^A & t_c < L \\ R_{t_a, t_c}^A & t_c \geq L \end{cases} \quad (42)$$

$$w_{t_b}(t_a) = \begin{cases} 0 & t_b < L \\ \frac{\delta_{t_a, t_b}}{\Delta t} & t_b \geq L \end{cases}. \quad (43)$$

4 Results

In this section we will first compare the results of the DMFT equations' numerical integration with the ones of the numerical simulation, in order to assert that the theory is correct. The discussion will then focus on the results of the numerical integration.

4.1 Comparison between DMFT and simulation

In order to verify the correctness of the DMFT equations, we compare the system's observables with the ones computed with a numerical simulation.

The simulation consists of considering a system of finite size N , big enough to see a mean field effect, where the degrees of freedom are updated at each time-step in the following way:

$$\mathbf{x}(t + \Delta t) = \sqrt{N} \frac{\mathbf{x}(t) - \Delta t \frac{\partial H}{\partial \mathbf{x}(t)}}{\left| \mathbf{x}(t) - \Delta t \frac{\partial H}{\partial \mathbf{x}(t)} \right|}. \quad (44)$$

The constraint $|\mathbf{x}(0)|^2 = N$ is satisfied by re-normalising \mathbf{x} at every time step. Here the initial condition is sampled from a flat distribution and, for each sample, the matrices J_{ij}^μ are sampled from a Gaussian distribution with zero mean and unit variance. Therefore, for each initial condition, we sample M J_{ij} matrices and we let the system evolve for L time steps with the dynamics in Eq. (44). We repeat this for a number of S samples.

The observables that we take into consideration for the comparison are the following:

- The correlation function $C(t, 0)$ computed in the simulation as:

$$C(t, 0) = \frac{1}{N} \mathbf{x}(t) \cdot \mathbf{x}(0) \quad (45)$$

This quantity measures how much the configuration of the system at time t is correlated with the initial configuration at time $t = 0$.

- The Lagrange multiplier $\mu(t)$ computed in the simulation as:

$$\mu(t) = -\frac{2}{N} \sum_{\mu=0}^M (h_{\mu}(t) - p_0) h_{\mu}(t). \quad (46)$$

- The average value of $h_{\mu}(t)$, which in the simulation is:

$$h(t) = \frac{1}{M} \sum_{\mu=0}^M h_{\mu}(t) \quad (47)$$

To compute $h(t)$ with DMFT, one can easily show that:

$$h(t) = \langle h(a) \rangle_{\mathcal{Z}_{dyn}} \Big|_{\text{scalar part}}. \quad (48)$$

and by promoting p_0 to a superfield $p_0(a)$ with a Grassmann variable, one has

$$\langle h(a) \rangle_{\mathcal{Z}_{dyn}} = \frac{\delta}{\delta p_0(a)} \ln \mathcal{Z}_{dyn} \Big|_{p_0(a)=p_0}. \quad (49)$$

Finally, by performing the calculations one finds:

$$p_0 - h(t) = p_0 \int_0^t dt' R_A(t, t'). \quad (50)$$

We also look at the behaviour of $|h(t) - p_0|$ because we expect it to be approaching zero, when the system reaches a zero energy configuration and a positive value, when instead the system reaches a local minimum of the Hamiltonian.

- The energy per degree of freedom, which in the simulation is

$$e(t) = \frac{1}{N} H(t). \quad (51)$$

while in the DMFT the energy is computed as

$$e(t) = \frac{\alpha}{2} (h(a) - p_0)^2 \quad (52)$$

which can be shown to be:

$$e(t) = \frac{\alpha}{2} \left[p_0^2 \left(\int_0^t dt' R_A(t, t') \right)^2 - C_A(t, t) \right]. \quad (53)$$

As a remark, one can also check the correlation of $h(t)$ for the simulation and the DMFT:

$$\langle h(t)h(t') \rangle - h(t)h(t') = \frac{1}{M} \sum_{\mu=0}^M h_{\mu}(t)h_{\mu}(t') - \frac{1}{M^2} \sum_{\mu, \nu=0}^M h_{\mu}(t)h_{\nu}(t') = -C_A(t, t') \quad (54)$$

In Fig. 3 we show the comparison done for $L = 2000$, $\Delta t = 0.025$ and $S = 1000$. We consider a system of size $N = 500$ and $M = 125$, since we are focusing on the case for $\alpha = 0.25$. As one can clearly see from the graphs, there is a good agreement between the numerical simulation and the

numerical integration of the DMFT equations, especially for $\mu(t)$, $C(t, 0)$ and $h(t)$ (see, respectively, Figs. 2d, 2c, 2b). For the energy, the agreement is good for small times but for small values of p_0 , as the energy approaches zero, it is no longer such, especially for values of energy under 10^{-3} (see Fig. 2a). This is certainly due to the finite size of the time step and a finite sample size S . One must also not forget that the theory is true for the mean field limit, $N \rightarrow \infty$, while the samples considered for the simulations have a finite size. Therefore, we would expect a perfect agreement for $S \rightarrow \infty$, $N \rightarrow \infty$ and $\Delta t \rightarrow 0$.

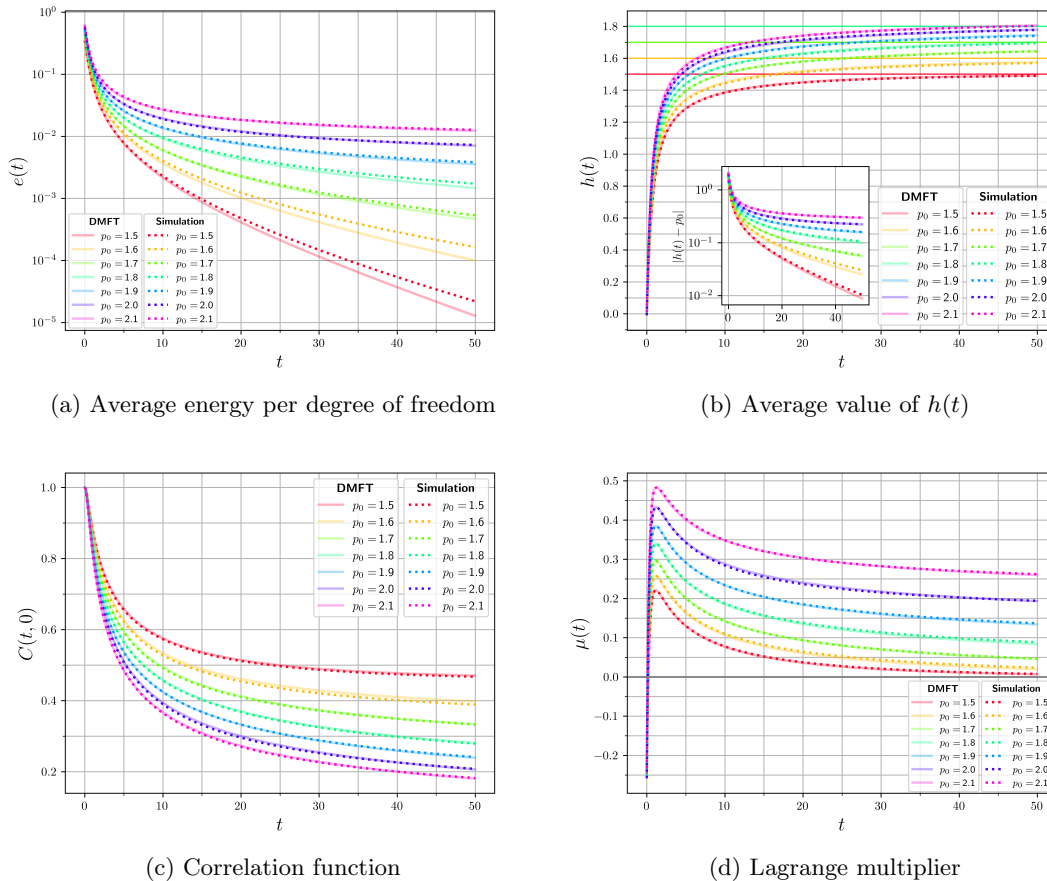


Figure 2: Comparison between the numerical simulation's and DMFT's results. The parameters used are $S = 1000$, $N = 500$, $M = 125$, $L = 2000$, $\Delta t = 0.025$ and $\alpha = 0.25$. The energy's plot (a) is in semi-log scale. The inset in plot (b) is the semi-log plot of $|h(t) - p_0|$.

4.2 Results of DMFT's numerical integration

In this section, we will analyse in depth the results of the DMFT equations' numerical integration. For this analysis, we choose $L = 4000$, $\Delta t = 0.05$ and different values of p_0 . First thing we notice, from all graphs, is that the rigidity transition for this model occurs for some value of p_0 in the interval $[1.8, 2.0]$. This is in accordance with the value of $p_J \simeq 1.871$ found in [9].

In Fig. 3a we plot the energy in logarithmic scale as a function of time. For $p_0 < 1.7$, the energy decays exponentially to the zero energy configuration, while for $p_0 > 1.7$, for long times, it reaches a plateau. By plotting $e(t)$ in log-log scale, see Fig. 3b, one can notice an almost power law behaviour

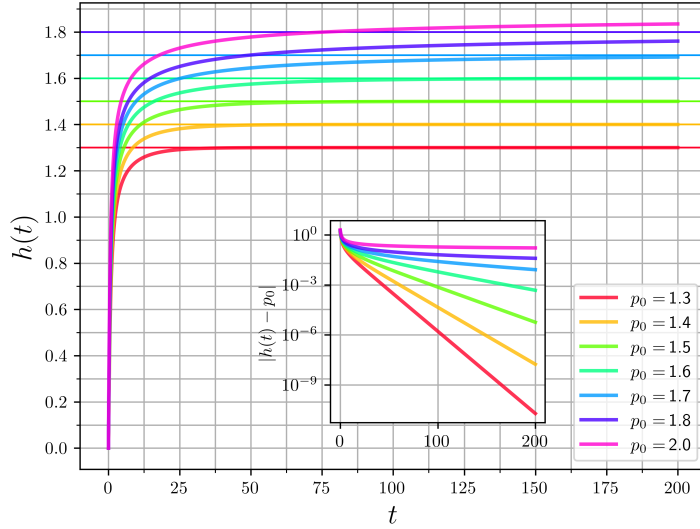
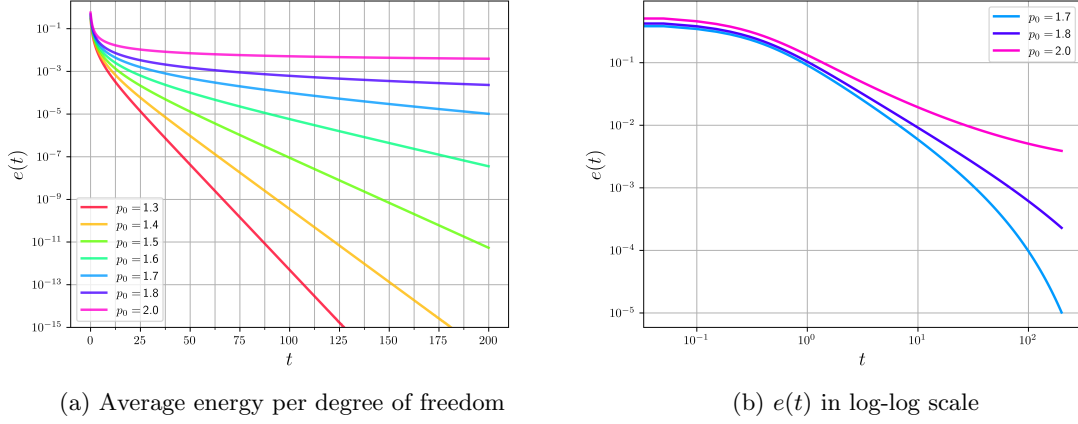
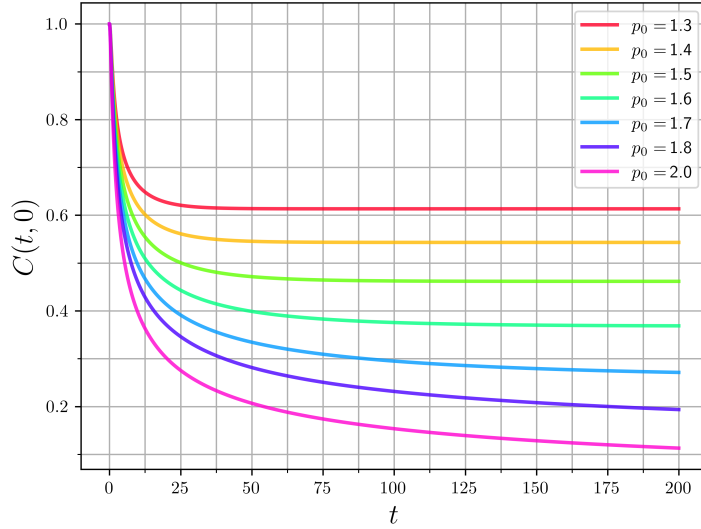


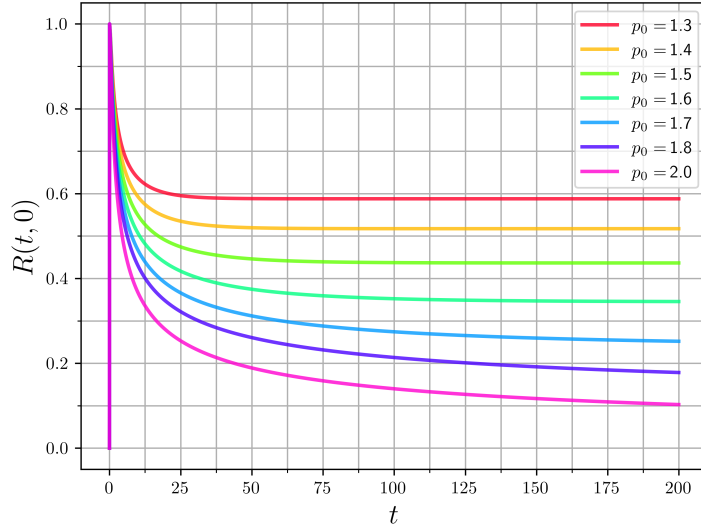
Figure 3: Results of the DMFT's numerical integration for parameters $L = 4000$, $\Delta t = 0.05$ and $\alpha = 0.25$. The energy's plot (a) is in semi-log scale. The inset in plot (c) is the semi-log plot of $|h(t) - p_0|$.

for $p_0 = 1.8$, which is expected at the critical point. A similar behaviour is seen for $|h(t) - p_0|$, as shown in the inset of Fig. 3c. Therefore, if the tissue is out-of-equilibrium but in the liquid phase, it quickly reaches the zero energy configuration. If instead is in the solid phase, it slowly relaxes towards a configuration of positive energy. In fact, for high values of p_0 the slope of $e(t)$ in log-scale is small.

In Fig. 3c, one sees that for $p_0 < 1.7$ $h(t)$ reaches quickly the target value p_0 , while for $p_0 > 1.7$ we would expect for $h(t)$ to reach some positive value different from p_0 , but one would have to check this for larger values of L . This behaviour shows how in the liquid phase all the constraints $h_\mu(\mathbf{x}) = p_0$ are satisfied, while this is not true in the solid phase. Note that the time for $h(t)$ to reach the target value increases with p_0 . In Fig. 4a, we plot the correlation function $C(t, 0)$: for



(a) Correlation function



(b) Response function

Figure 4: Correlation and response function obtained from the DMFT'S numerical integration. The parameters used are $L = 4000$, $\Delta t = 0.05$ and $\alpha = 0.25$

$p_0 < 1.7$, the correlation decays very quickly towards a positive valued plateau, meaning that during the dynamics the system does not completely decorrelate from its initial condition. Thus, for a small p_0 , confluent tissues tend to retain memory of their initial state. This can be intuitively explained in the following way: $h(0) = h(\mathbf{x}(0))$ is a Gaussian random variable with mean zero, thus we would expect that the typical value of h at time zero is very close to p_0 , which is small. Therefore, the

system does not have to search for long before it finds the configuration at minimum energy. For increasing p_0 , the relaxation time increases while the value of the plateau decreases: the final state is more and more decorrelated from the initial state for higher values of p_0 . As we reach $p_0 = 1.8$, one may guess that $C(t, 0)$ reaches zero but due to its slow decay, further investigation is necessary, either by increasing L or through extrapolation.

Finally, in Fig. 4b, we plot the response function $R(t, 0)$ that quantifies the effect of a linear perturbation on the system at $t = 0$ on the state of the system at time $t > 0$. The behaviour is similar to the one of $C(t, 0)$: a fast decay towards a positive plateau for small values of p_0 and a slow decay, probably towards zero, one must check this, at higher values of p_0 .

5 Digression: gradient descent dynamics and RSB

We recall that the equations of the DMFT have been derived starting from the dynamics dictated in Eq. (5). Without the context of confluent tissues, this is simply the dynamics of a gradient descent. A gradient descent algorithm is a method for finding minima, both local and global, of a function $H(\mathbf{x})$. It is largely used in the context of machine learning for minimising the cost function of a neural network. A neural network is a device that can be trained in order to predict a label of some kind of input. For example, a typical task of a neural network is the classification of images of objects/animals. In order to train the neural network, one has a dataset of inputs and outputs and the goal is to find the weights to be assigned to the links of the neural network. In order to do this, one has to minimise a cost function and an algorithm that performs this is the gradient descent and its variants.

The dynamics of gradient descent algorithms has been largely studied, especially because its effectiveness in finding global minima is fundamental for learning. In fact, the gradient descent algorithm does not guarantee to find global minima and it is possible that it may get stuck in some local minimum of the cost function, see [22] for an example of a study on gradient descent dynamics. Our model shades some light on the dynamics of the gradient descent algorithm. In particular, it confirms that it is blind to replica symmetry breaking (RSB) when it occurs at zero temperature. We recall that RSB occurs when the loss function becomes a complex landscape of saddles, minima and maxima such that also metastable states contribute to equilibrium configurations of the system [8, 25]. In short, ergodicity is broken. If the RSB happens at finite temperature, this may be a problem for search algorithms because they end up stuck in some local minima of the complex landscape. For our model, RSB at zero temperature occurs in the liquid/SAT phase $p_0^G = 1$ but the gradient descent is still able to reach the true minimum of the system, as its clearly shown in the Fig. 3a for $p_0 < 1.7$.

6 Conclusion

In this paper, we have re-proposed a simple mean field model for biological tissue that is exactly solvable and we have studied its dynamical properties to shed some light on the dynamics of tissues at zero temperature. Throughout the dynamical study, we have confirmed the existence of a jamming transition for a value of $p_0 \in [1.8, 2.0]$ and, in the context of deep learning, we have shown that zero temperature RSB has no effect on gradient descent dynamics. A more rigorous analysis of the jamming transition is required as the critical value p_J in the dynamical case may be algorithm-dependant and different from the equilibrium case.

In addition, we have developed, both analytically and numerically, a simple mean field model that in future work can be enriched with additional parameters and non-conservative forces. In particular, it would be interesting to understand what happens to the dynamics when one adds an out-of-equilibrium noise, since we cannot predict what is the stationary probability distribution of the gradient descent dynamics nor we can know if such stationary measure exists. Such study

would be very useful in the context of confluent tissues and allow a qualitative comparison with the dynamical properties of Vertex/Voronoi models and experimental data. Instead, in the context of optimisation science, we have built a solid set-up for studying other quadratic Hamiltonians. In fact, the equations and the code of this model have been adapted to a different Hamiltonian in [26], in order to show how stochastic gradient descent is more efficient than simple gradient descent in recovering a non-linearly encrypted signal.

References

- [1] Pierre-François Lenne and Vikas Trivedi. “Sculpting tissues by phase transitions”. In: *Nature Communications* 13.1 (Feb. 2022). DOI: [10.1038/s41467-022-28151-9](https://doi.org/10.1038/s41467-022-28151-9).
- [2] Thomas E. Angelini et al. “Glass-like dynamics of collective cell migration”. In: *Proceedings of the National Academy of Sciences* 108.12 (Feb. 2011), pp. 4714–4719. DOI: [10.1073/pnas.1010059108](https://doi.org/10.1073/pnas.1010059108).
- [3] Kenechukwu David Nnetu et al. “The impact of jamming on boundaries of collectively moving weak-interacting cells”. In: *New Journal of Physics* 14.11 (Nov. 2012), p. 115012. DOI: [10.1088/1367-2630/14/11/115012](https://doi.org/10.1088/1367-2630/14/11/115012).
- [4] Eliane Blauth et al. “Jamming in Embryogenesis and Cancer Progression”. In: *Frontiers in Physics* 9 (Aug. 2021). DOI: [10.3389/fphy.2021.666709](https://doi.org/10.3389/fphy.2021.666709).
- [5] Jin-Ah Park et al. “Unjamming and cell shape in the asthmatic airway epithelium”. In: *Nature Materials* 14.10 (Aug. 2015), pp. 1040–1048. DOI: [10.1038/nmat4357](https://doi.org/10.1038/nmat4357).
- [6] Matthias Merkel and M Lisa Manning. “A geometrically controlled rigidity transition in a model for confluent 3D tissues”. In: *New Journal of Physics* 20.2 (Feb. 2018), p. 022002. DOI: [10.1088/1367-2630/aaaa13](https://doi.org/10.1088/1367-2630/aaaa13).
- [7] Silvio Franz and Giorgio Parisi. “The simplest model of jamming”. In: *Journal of Physics A: Mathematical and Theoretical* 49.14 (Feb. 2016), p. 145001. DOI: [10.1088/1751-8113/49/14/145001](https://doi.org/10.1088/1751-8113/49/14/145001).
- [8] Pierfrancesco Urbani. *Statistical Physics of glassy systems: tools and applications*. 2018.
- [9] Pierfrancesco Urbani. “A continuous constraint satisfaction problem for the rigidity transition in confluent tissues”. In: *Journal of Physics A: Mathematical and Theoretical* 56.11 (Feb. 2023), p. 115003. DOI: [10.1088/1751-8121/acb742](https://doi.org/10.1088/1751-8121/acb742).
- [10] Persia Jana Kamali and Pierfrancesco Urbani. *Dynamical mean field theory for models of confluent tissues and beyond*. 2023. DOI: [10.48550/ARXIV.2306.06420](https://doi.org/10.48550/ARXIV.2306.06420).
- [11] Alexander G. Fletcher et al. “Vertex Models of Epithelial Morphogenesis”. In: *Biophysical Journal* 106.11 (June 2014), pp. 2291–2304. DOI: [10.1016/j.bpj.2013.11.4498](https://doi.org/10.1016/j.bpj.2013.11.4498).
- [12] Dapeng Bi et al. “Motility-Driven Glass and Jamming Transitions in Biological Tissues”. In: *Phys. Rev. X* 6 (2 Apr. 2016), p. 021011. DOI: [10.1103/PhysRevX.6.021011](https://doi.org/10.1103/PhysRevX.6.021011).
- [13] Bi Dapeng et al. “A density-independent rigidity transition in biological tissues”. In: *Nature Physics* 11.12 (Dec. 2015), pp. 1074–1079. ISSN: 1745-2481. DOI: [10.1038/nphys3471](https://doi.org/10.1038/nphys3471).
- [14] Carl-Philipp Heisenberg and Yohanns Bellaïche. “Forces in Tissue Morphogenesis and Patterning”. In: *Cell* 153.5 (May 2013), pp. 948–962. DOI: [10.1016/j.cell.2013.05.008](https://doi.org/10.1016/j.cell.2013.05.008).
- [15] T C Lubensky et al. *Phonons and elasticity in critically coordinated lattices*. 2015. arXiv: [1503.01324](https://arxiv.org/abs/1503.01324) [[cond-mat.soft](https://arxiv.org/abs/1503.01324)].
- [16] Matthias Merkel et al. “A minimal-length approach unifies rigidity in underconstrained materials”. In: *Proceedings of the National Academy of Sciences* 116.14 (Mar. 2019), pp. 6560–6568. DOI: [10.1073/pnas.1815436116](https://doi.org/10.1073/pnas.1815436116).

- [17] Cristopher Moore and Stephan Mertens. *The Nature of Computation*. OUP -Oxford, 2011.
- [18] Silvio Franz, Antonio Sclocchi, and Pierfrancesco Urbani. “Critical Jammed Phase of the Linear Perceptron”. In: *Physical Review Letters* 123.11 (Sept. 2019). DOI: [10.1103/physrevlett.123.115702](https://doi.org/10.1103/physrevlett.123.115702).
- [19] Leticia F. Cugliandolo. *Dynamics of glassy systems*. 2002. arXiv: [cond-mat/0210312](https://arxiv.org/abs/cond-mat/0210312) [[cond-mat](#)].
- [20] John A. Hertz, Yasser Roudi, and Peter Sollich. “Path integral methods for the dynamics of stochastic and disordered systems”. In: *Journal of Physics A Mathematical General* 50.3, 033001 (Jan. 2017), p. 033001. DOI: [10.1088/1751-8121/50/3/033001](https://doi.org/10.1088/1751-8121/50/3/033001). arXiv: [1604.05775](https://arxiv.org/abs/1604.05775) [[cond-mat.dis-nn](#)].
- [21] Francesca Mignacco, Pierfrancesco Urbani, and Lenka Zdeborová. “Stochasticity helps to navigate rough landscapes: comparing gradient-descent-based algorithms in the phase retrieval problem”. In: *Machine Learning: Science and Technology* 2.3 (July 2021), p. 035029. DOI: [10.1088/2632-2153/ac0615](https://doi.org/10.1088/2632-2153/ac0615).
- [22] Francesca Mignacco et al. “Dynamical mean-field theory for stochastic gradient descent in Gaussian mixture classification*”. In: *Journal of Statistical Mechanics: Theory and Experiment* 2021.12 (Dec. 2021), p. 124008. DOI: [10.1088/1742-5468/ac3a80](https://doi.org/10.1088/1742-5468/ac3a80).
- [23] Elisabeth Agoritsas et al. “Out-of-equilibrium dynamical mean-field equations for the perceptron model”. In: *Journal of Physics A: Mathematical and Theoretical* 51.8 (Jan. 2018), p. 085002. DOI: [10.1088/1751-8121/aaa68d](https://doi.org/10.1088/1751-8121/aaa68d).
- [24] J. Zinn-Justin. *Quantum Field Theory and Critical Phenomena*. International series of monographs on physics. Oxford University Press, 2021. ISBN: 9780198834625. URL: <https://books.google.fr/books?id=ioskEAAAQBAJ>.
- [25] Tommaso Castellani and Andrea Cavagna. “Spin-glass theory for pedestrians”. In: *Journal of Statistical Mechanics: Theory and Experiment* 2005.05 (May 2005), P05012. DOI: [10.1088/1742-5468/2005/05/p05012](https://doi.org/10.1088/1742-5468/2005/05/p05012).
- [26] Persia Jana Kamali and Pierfrancesco Urbani. *Stochastic Gradient Descent outperforms Gradient Descent in recovering a high-dimensional signal in a glassy energy landscape*. 2023. arXiv: [2309.04788](https://arxiv.org/abs/2309.04788) [[cs.LG](#)].